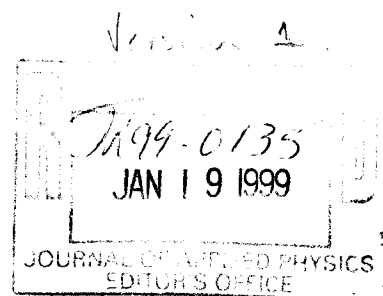


Highly Sensitive Quantum Well Infrared Photodetectors

Tom Cwik and C. Yeh

*Jet Propulsion Laboratory
California Institute of Technology
4800 Oak Grove Dr., Pasadena, CA 91109*



Abstract

A fundamentally new method for light coupling in quantum well infrared photodetectors that provides a 10-fold improvement over an optimized grating coupler is presented. It is based on the prism-film coupler concept developed earlier for selective mode coupling into integrated optical circuits. In this paper this concept is specifically used to turn the incident electric field from one that is polarized parallel to the quantum well layer to one that is mostly perpendicular to the layer, thereby increasing dramatically the sensitivity of the quantum well infrared photodetector. Detailed sample design and its computer simulation results are given and discussed.

I. Introduction

A limitation of quantum well infrared photodetectors is that they can only detect (absorb) infrared light whose electric field is polarized in a direction which is perpendicular to the plane of the quantum well layers [1]. The incident infrared light usually takes the form of a plane wave whose electric field is polarized in a direction that is parallel to the plane of the quantum well layers. Therefore, much effort has been focused on ways to induce the generation of electric fields having the desired polarization.

Historically, a direct approach for light coupling is to orient the quantum well infrared photodetector at a forty-five degree angle to the incident infrared radiation. The incident electric field will have a component ($1/\sqrt{2}$ of the incident electric vector) that can produce absorption of photons, and any additional scattering due to the mesa structure can enhance this absorption [2]. When the photodetectors are used in focal plane arrays, the photodetector array is oriented perpendicular to the scene to be imaged, the direction of propagation is perpendicular to the photodetector, and the electric vector is parallel to the quantum well layers. No absorption is possible in this orientation. To produce absorption in this focal plane array application, different structures have been developed. One structure uses a random surface at the base of the mesa structure to scatter the incident radiation into the correct polarization for absorption. Substantial enhancement in quantum well infrared photodetector responsivity compared to the forty-five degree incidence structure has been reported [3]. To improve upon the random surface grating, a variety of grating couplers has been developed [4,5]. These couplers consist of one or two-dimensional periodic profiles designed into the base of the mesa structure to convert the normally incident radiation to waves propagating parallel to the quantum well layers. For metallic profiles, an efficient grating design minimizes the energy reflected into the (0,0) harmonic, while maximizing the energy coupled into the propagating (± 1 , ± 1) harmonics that have a component of the electric field perpendicular to the quantum well layers. If the design operates just at the point of propagation of these first harmonics, the propagation vector is exactly parallel to the quantum well layers and maximum coupling can be achieved. This theoretical performance is achieved for infinite gratings, and is modified for finite sized gratings and when truncation effects and scattering due to the finite mesa size are considered. The performance of these grating structures can be enhanced to reduce the dark current associated with the quantum well structure, by patterning the multi-quantum

well layers, removing some of the wells [6]. To date the optimized grating coupled quantum well infrared photodetector offers the best performance.

The purpose of this paper is to show a new way to improve performance and that a 10-fold improvement over an optimized grating coupler is attainable. This new way is based on the prism-film coupler concept developed earlier for selective mode coupling into integrated optical circuits. In this paper, this concept is specifically used to turn the incident electric field from one that is polarized parallel to the quantum well layer to one that is mostly perpendicular to the layer, thereby increasing dramatically the sensitivity of the quantum well infrared photodetector. A detailed description on how this is accomplished will first be given. Computer simulations were carried out for several specific geometries corresponding to achievable practical designs. Figure of merits for these cases as well as that for an optimized 50 μm grating for the band between 14 μm and 16 μm will be given. Finally, we shall discuss the viability of the new design as a practical quantum well infrared photodetector device.

II. The Evanescent-Wave Prism-Film Coupler Concept

To efficiently couple light into dielectric waveguides and excite a given mode for integrated optic applications, evanescent-wave prism couplers were developed 30 years ago [7,8]. By feeding a light beam into a film through a broad surface of the film, one avoids the difficult problem of focusing a light beam through a rough film edge. Since the film and the prism are coupled over a length of many optical wavelengths, energy is transferred continuously between them as waves propagate over the coupling region and as shown in [7], very high coupling efficiency can be obtained. In this paper our goal is to change the polarization of an incident wave from a direction which is parallel to the quantum well layers to a direction which is normal to the layers. It will be shown below that this evanescent-wave prism film coupler is capable of providing this transformation.

Shown in Figure 1 is an evanescent-wave prism-film coupler. A plane wave with the electric field polarized parallel to the substrate layers is incident on the prism. It enters the prism and is totally reflected at or near the critical angle at the base of the prism. Because of the total reflection, the field in the prism is a standing wave and the field beyond the base of the prism is an exponentially decaying evanescent field that decreases rapidly away from the prism surface. As seen from Figure 1, the prism, placed on top of the quantum well layers, maintains a small uniform air gap between the base surface of the prism and the top surface of the layers. The evanescent field below the prism then penetrates into the layers and excites a surface wave into the layers. When the gap thickness t and relative indices are tuned appropriately, up to 80% of the incident radiation can be coupled into a mode within the dielectric layer [7]. For the critical angle to be reached, $n_p < n_g$, and for a guided wave to be supported in the dielectric layer, $n_{QW} > n_g, n_s$ where the indices of refraction n_p, n_g, n_{QW} and n_s are of the prism, gap, guided wave and substrate layers respectively. The prism is truncated at some distance along the path of coupling to eliminate energy being coupled back into the prism along the direction of propagation.

Furthermore, one may note from Figure 1 that the electric field component of the evanescent field below the prism is now normal to the bottom surface of the prism. This means that the electric field component of the incident wave has been successfully transformed to the direction needed by the quantum well infrared photodetector layers for efficient absorption.

It is noted that several factors govern the response of this quantum well infrared photodetector. They include the angle of the prism, the index of the prism, the indices and the thickness of the quantum well layers, the separation of the air gap and the length of the coupling region. Proper adjustment of these factors produces the desired design.

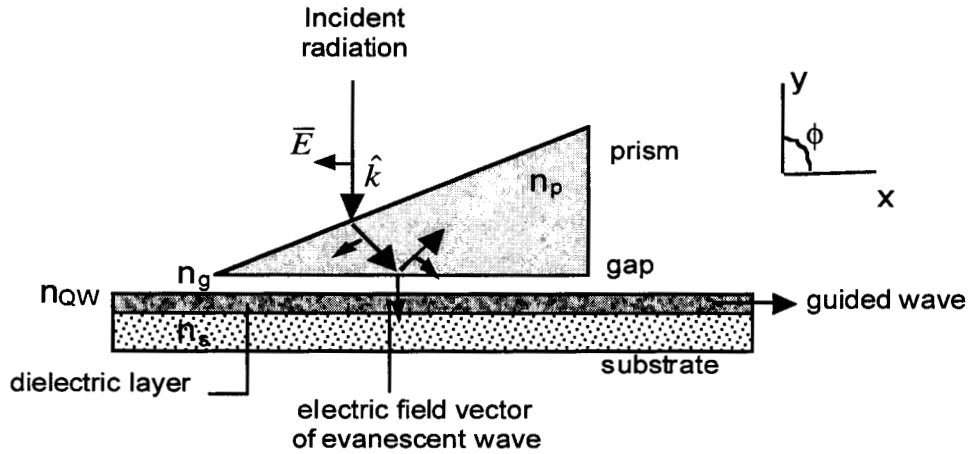


Figure 1 Geometry of prism coupler for integrated optics application. Solid lines indicate direction of propagation; smaller arrows indicate electric field vector. The electric vector of the evanescent wave is polarized vertically. The indices of refraction n_p , n_g , n_{QW} and n_s are of the prism, gap, guided wave and substrate layers respectively.

III. Analysis

The above description of the evanescent-wave coupler is based on an optical modal analysis since the size of the prism thin-film coupler is electrically large. In this paper, the infrared coupler is much smaller in size, operating in the resonant-length regime. Therefore, a direct solution of Maxwell's equations throughout the device is necessary. A method that couples a finite element solution of Maxwell's equations inside the device with an integral equation representation of the fields on the boundary of the finite element mesh is used. The integral equation includes the radiation boundary condition to accurately truncate the computational domain. By coupling the two representations at the surface, a system of equations that describes the fields throughout the device is found.

A complete description of the numerical approach is found in [9]. The analysis considers a two-dimensional scattering geometry consisting of an interior and exterior regions bounded by a surface. The surface S , taken to lie on the boundary of the device, divides the geometry into interior region V and

exterior region Ω . Volume V can be inhomogeneous, containing lossy material and perfect conductors that can lie partly on the surface S , therefore modeling the device materials accurately. The magnetic field is polarized in the z direction and is produced by an incident magnetic field

$$H^{inc}(\rho) = \hat{z} e^{jk(x\cos(\phi) + y\sin(\phi))} e^{j\alpha x} \quad (1)$$

due to a source in the exterior region Ω . The incident magnetic field is denoted H^{inc} , k is the wavenumber, ϕ is the polar angle (see Figure 1), and the time dependence is $e^{j\alpha x}$.

III.A The Wave and Integral Equations

In the inhomogeneous region V , the wave equation for the total magnetic field $H = \hat{z}H_z$

$$\nabla \times \frac{1}{\epsilon_r(\rho)} \nabla \times H(\rho) - \mu_r(\rho) k^2 H(\rho) = 0 \quad \rho \in V \quad (2)$$

is used; ρ is the two-dimensional position vector. Both ϵ_r and μ_r are functions of position and may be complex, i.e., $\epsilon_r = \epsilon' - j\epsilon''$ and $\mu_r = \mu' - j\mu''$, to account for dielectric and magnetic loss. In the homogenous exterior region Ω , the surface magnetic field integral equation [10]

$$H(\rho) = 2H^{inc}(\rho) + \frac{jk}{2} \oint_{\partial V} H_{tan}(\rho') H_1^{(2)}(k|\rho - \rho'|) \cos(\hat{n}', \rho - \rho') dl' + \frac{\omega\epsilon}{2} \oint_{\partial V} E_{tan}(\rho') H_0^{(2)}(k|\rho - \rho'|) dl' \quad \rho, \rho' \in S \quad (3)$$

is used; $H_{tan} = \hat{n} \times H^+$ and $E_{tan} = \hat{n} \times E^+$ are the tangential field components just exterior to the surface ∂V . $H_0^{(2)}$ and $H_1^{(2)}$ are the outgoing first and second order

Hankel functions; $(\hat{n}', \rho - \rho')$ denotes the angle between source and observation points ρ and ρ' respectively, and principal value integrations are implied.

III.B Boundary Condition Enforcement

With an equation written for the fields interior to the volume, and one also written for the fields on the surface that satisfies the radiation condition, it is only necessary to enforce boundary conditions to fully satisfy Maxwell's equations. Boundary conditions must be satisfied at all material boundaries, at infinity, and at the boundary surface of the two solutions (S). At material boundaries, which only reside within V , boundary conditions are satisfied in the finite element solution by a proper choice of elements, or by explicitly zeroing tangential electric field components to model perfectly conducting surfaces. As noted above, in the integral equation (3) the Sommerfeld radiation condition is naturally enforced by the outgoing Green's function. The only boundary conditions remaining need be satisfied at the surface S . Equating tangential electric field components gives

$$E_{\text{tan}}(\rho) + \frac{1}{j\omega\epsilon} \hat{n} \times \nabla \times H(\rho) = 0 \quad \rho \in S \quad (4)$$

on the surface S . If part of the surface encloses a perfect conductor, $H(\rho)$ within the conductor is identically zero, and the usual boundary condition $E_{\text{tan}} = 0$ applies. Similarly, equating tangential magnetic field components gives

$$H_{\text{tan}}(\rho) - \hat{n} \times H(\rho) = 0 \quad \rho \in S \quad (5)$$

on the surface S .

III.C Discretization

The wave (2) and integral equations (3), as well as boundary conditions (4) and (5), are combined into three equations. This system of equations is discretized and solved numerically yielding the magnetic fields in the interior region and tangential magnetic and electric fields on the surface S .

For a finite element solution of the wave equation, (2) is dotted against a testing function $T = \hat{z}T_z$, integrated over the volume, and integrated again by parts yielding the weak form

$$\int_V \left[\frac{1}{\epsilon_r} \nabla T_z \cdot \nabla H_z - \mu_r k^2 T_z \cdot H_z \right] dv + \int_{\partial V} \frac{1}{\epsilon_r} T \cdot [\hat{n} \times \nabla \times H] ds \quad (6)$$

The boundary condition on tangential components of the electric field (4) is combined into this equation by noting that in the contour integral in (6), $\hat{n} \times \nabla \times H = j\omega\epsilon E_{\tan}$; therefore, substituting (4) into this integral gives

$$\int_V \left[\frac{1}{\epsilon_r} \nabla T_z \cdot \nabla H_z - \mu_r k^2 T_z \cdot H_z \right] dv - j\omega\epsilon_0 \int_{\partial V} T_z E_{\tan} ds \quad (7)$$

for the first equation of the system ($E_{\tan} = \hat{t}E_{\tan}$, \hat{t} is the surface tangent). The second equation is found by enforcing (5) in a weak sense, i.e., dotting (5) against a testing function U and integrating

$$\int_{\partial V} U \cdot [\hat{n} \times H(\rho) - H_{\tan}] ds = 0 \quad (8)$$

The third and final equation of the system is found from a standard moment solution to (3), dotting the equation against a testing function W and integrating

along the contour S. This equation will not be written explicitly, the reader is referred to the method of moments literature [e.g. 11] for further details.

Equations (7), (8), and (3) tested against W , are discretized, forming the system of matrix equations

$$\begin{bmatrix} K & C & 0 \\ C^t & 0 & T \\ 0 & G_e & G_h \end{bmatrix} \begin{bmatrix} H \\ E_{\tan} \\ H_{\tan} \end{bmatrix} = \begin{bmatrix} 0 \\ 0 \\ V^{inc} \end{bmatrix} \quad (9)$$

where K is the square sparse matrix resulting from the volume integral of (7); its order is the number of nodes in the finite element grid. C and T are coupling matrices found from evaluating (8) (C^t denotes the transpose) and G_e and G_h are moment method matrices found from the discretization of (3). The solution of the linear system (9) produces the magnetic field H everywhere inside the device, and the tangential fields E and H on the surface. Numerical convergence of the solution is confirmed by successively finer discretizations of the finite element mesh. Accuracy studies and comparisons to measurements for a range of objects can be found in [9].

IV. Computer Simulation Results

A finite element mesh is generated over the prism coupler structure. A 2-dimensional simulation (a cut in the x - y plane) is performed, solving for the z component of the magnetic field, H_z , due to the incident plane wave. Since it is the y component of the electric field, E_y that induces absorption of photons in the quantum well layers, the electric field is calculated from magnetic field using an interpolation method [12]. To measure the effectiveness of the absorption of the incident radiation, the magnitude squared of E_y is calculated and integrated over the quantum well layer. This is the figure of merit that is used to compare with other methods. The figure of merit is defined as

$$F = \iint |E_y(x, y)|^2 dx dy \quad (10)$$

where the integral is over the active region.

For the quantum well infrared photodetector coupler, the substrate layer shown in Figure 1 is replaced by a metal layer and the active region is placed directly below the prism (Figure 2). The dimensions and materials used in the design are shown in the Table in Figure 2 for optimized absorption at 15 μ m.

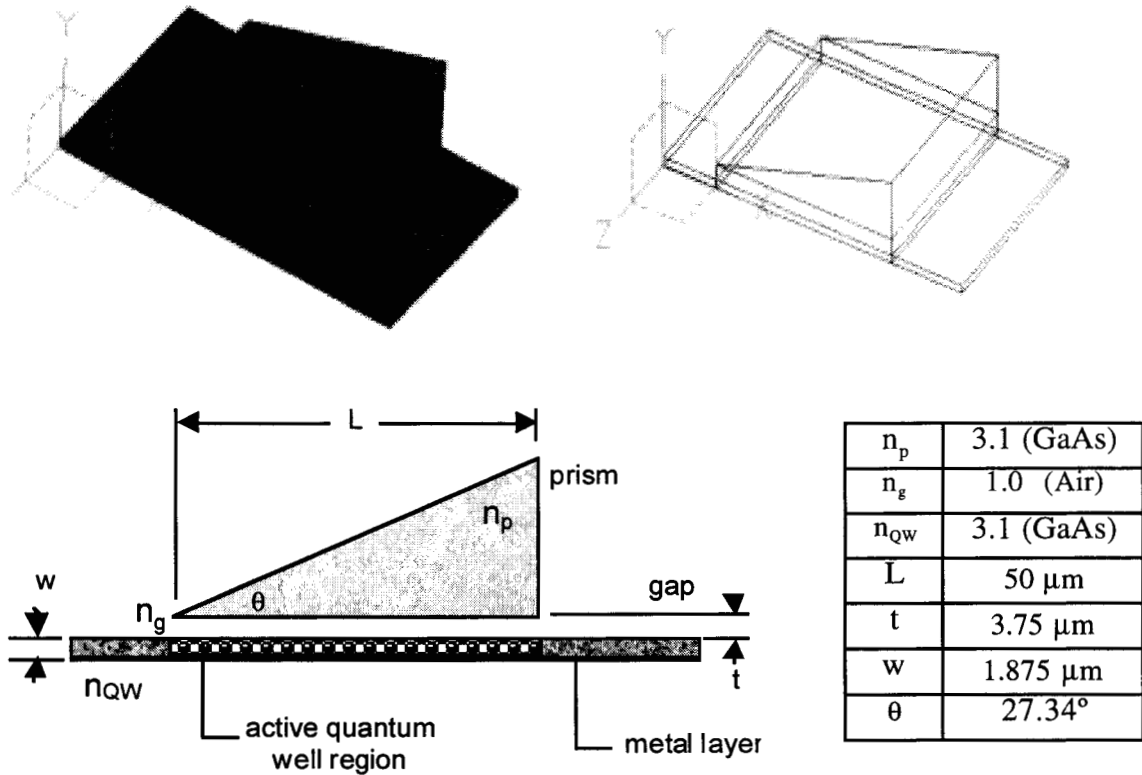


Figure 2. Geometry of prism coupler for light coupling application. The top figures show the three-dimensional structure. The geometry and variables are shown to the lower left with the design values shown in the Table to the lower right. The prism length is L , the prism angle is θ ; the gap and active gallium arsenide thickness' are t and w respectively. The indices of refraction n_p , n_g , n_{QW} are of the prism, gap and quantum well layers respectively.

For this design, the quantum well layer is $50\mu\text{m}$ by $1.875\mu\text{m}$. The prism angle θ , based on the optical design outlined in Section II is chosen to provide a totally reflected wave when the incident plane wave reaches the bottom surface of the prism.

Shown in Figure 3 is a plot of the figure of merit as a function of wavelength for the prism coupler shown in Figure 2. The results show several peaks in the figure of merit indicating that very efficient absorption occurs at those wavelengths. The presence of these peaks is not surprising since the quantum well layer waveguide is truncated (terminated) at both ends forming a surface waveguide resonator with specific resonant frequencies. The layer is truncated to both contain the energy for increased absorption and to isolate one element from another when this structure is used as a single pixel in a focal plane array. The multiple resonances though were not found to be dependent on a single dimension of the structure. Rather they depend upon a combination of the prism angle, gap thickness and thickness of the quantum well substrate. Also noted is the fact that the absorption peaks are not uniform in magnitude due to the frequency dependence of the prism-waveguide coupling effect. For the chosen specific parameters, the highest absorption peak occurs at $14.95\mu\text{m}$. What is surprising is the height of this peak; it is ten times higher than the highest valley where the highest valley is already comparable to the best figure of merit of an optimized grating coupler. The wavelength location of this peak can be adjusted by changing the prism angle, the thickness of the air gap, or the thickness of the quantum well substrate. The ultra sensitivity achievable by this prism-coupled quantum well infrared photodetector device is its most distinguishing feature. As a comparison, plotted in Figure 3 is the figure of merit for a grating structure consisting of a $50\mu\text{m}$ mesa with 10 grating periods and an active quantum well region of size $50\mu\text{m}$ by $3.75\mu\text{m}$ in cross section. It is seen that at the resonant wavelengths, the figure of merit for the prism-coupled quantum well infrared photodetector is far greater than that for the grating structure.

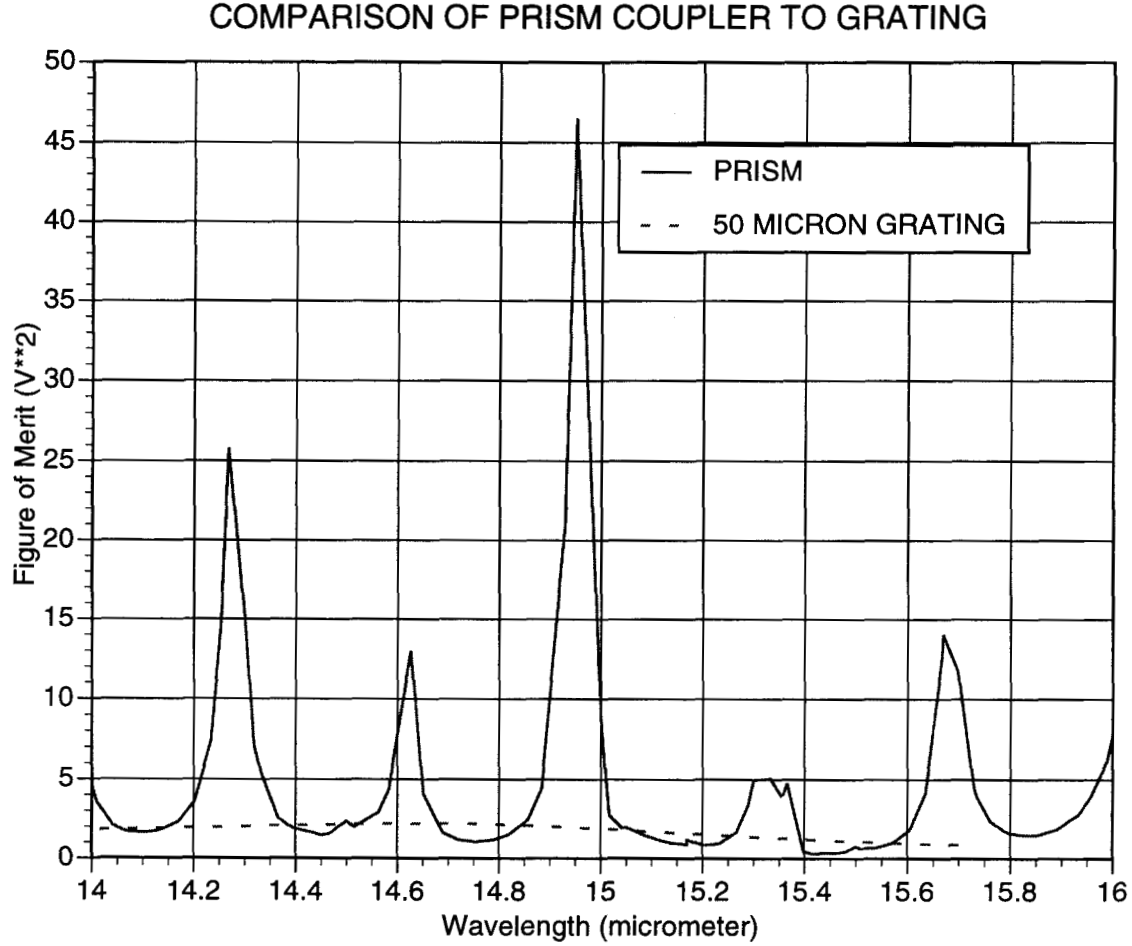


Figure 3. Comparison of figures of merit for the prism coupler shown in Figure 2 to that of an optimized 50 μm grating coupler. The figure of merit is defined in (10).

To further understand the prism coupled quantum well infrared photodetector, the distribution of the magnitude of E_y inside the prism, the air gap and the quantum well layer is obtained and displayed in Figures 4-6 for three different wavelengths (14.950 μm , 15.150 μm , and 14.267 μm). When the incident radiation is at 14.950 μm , according to Figure 3, the figure of merit is at a maximum indicating that most of the incident parallel polarized field has been transformed to vertically polarized field inside the quantum well layer. Hence, as expected, Figure 4 shows concentration of high magnitude E_y field (red) inside the quantum well layer. When the incident radiation is at 15.150 μm , according to Figure 3, the figure of merit is at a minimum indicating that only a

limited amount of the incident parallel polarized field has been transformed to vertically polarized field inside the quantum well layer. Hence, only low magnitude E_y (blue) is shown inside the (active) quantum well layer, while higher magnitude E_y (green) is found inside the (inactive) prism. The next figure is for incident radiation at 14.267 μm , another relative peak in the figure of merit in Figure 3, and a wavelength indicating good absorption by the quantum well layer. Figure 6 shows this situation, where, as expected, concentrations of high magnitude E_y field (red) inside the quantum well layer are found. It is seen that an excellent transformation of parallel polarized incident radiation to concentrations of vertically polarized radiation inside the quantum well layer can occur using this prism coupler technique.

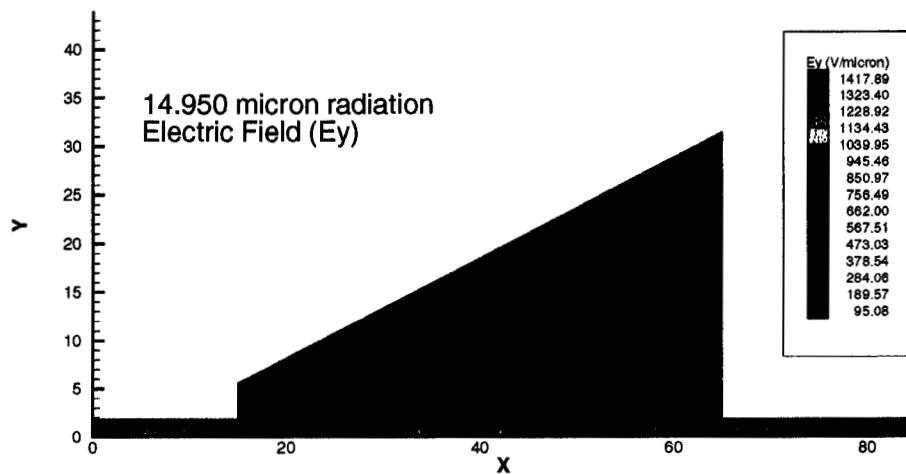


Figure 4. Field display at 14.950 μm radiation. The quantum well active region is directly below the prism. The wavelength of operation is at a relative peak in the figure of merit in Figure 3.

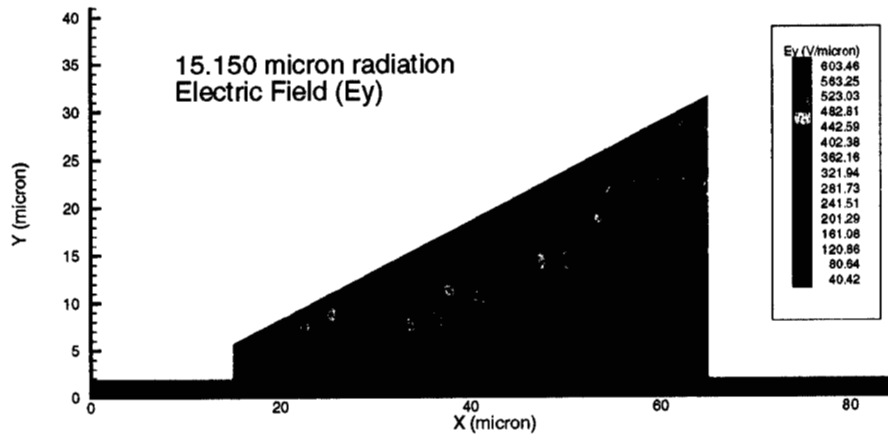


Figure 5. Field display at 15.150 μm radiation. This is at a null of the figure of merit indicating little coupling. Note the scale is also lower on this plot than on Figures 4 and 6. The quantum well active region is directly below the prism.

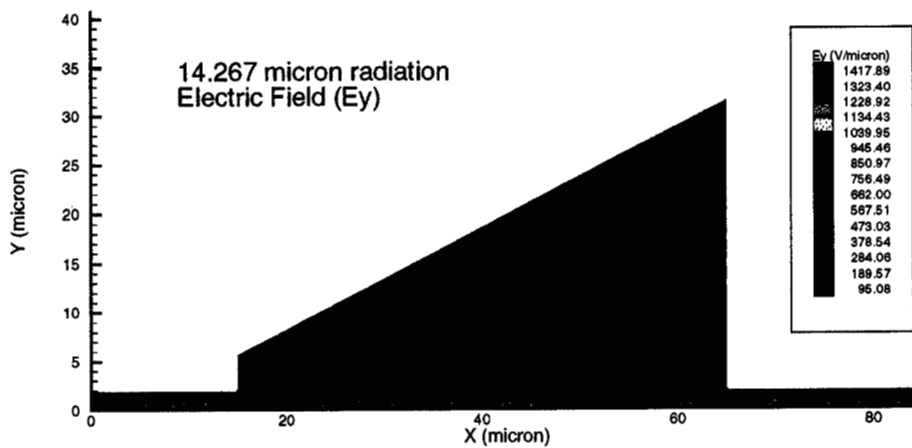


Figure 6. Field display at 14.267 μm radiation. This is a relative maximum of the figure of merit. The quantum well active region is directly below the prism.

VI. A Monolithic Design

The above design can be limiting due to the necessity of an air-gap layer between the prism and the active gallium arsenide layer. Fabrication difficulties as well as practical lifecycle limitations of the air-gap layer when the sensor is used in a space environment can limit its usefulness. To remedy this, a design consisting of gallium arsenide for the prism, aluminum gallium arsenide for the gap region and active gallium arsenide for the quantum well layer is used. The quantum well layer is placed on top of a gold base. This design allows monolithic fabrication since two materials with relatively uniform lattice constants and the greatest differences in their index of refraction are used [13]. To produce a more compact design, the right-angle prism was changed to a pyramid design, thus limiting its height. Dimensions and material parameters are shown in Figure 7. Because of the choice of materials as well as the resonant size of the device, the performance of this prism coupled quantum well infrared photodetector must be calculated using the exact wave equation approach discussed in Section III rather than the more intuitive ray optics approach discussed in Section II. In spite of the replacement of the air gap by a layer of aluminum gallium arsenide, substantial coupling of the desired polarized field will still take place resulting in dramatic increase in the sensitivity of this photodetector at certain wavelengths.

Shown in Figure 8 is the figure of merit for designs with two different gap widths, compared to the grating coupler design. It is noted that nearly uniformly periodic resonant character of the figure of merit has disappeared and the overall level is higher than the air-gap design. It is clear that sharp resonances can be produced from the air-gap optical design, while these are smoothed when the higher index aluminum gallium arsenide gap is used and the prism angle is reduced from the optimum optical design of 76° to the 48° design in Figure 7. Similarly a resonance does not exist at $15\text{ }\mu\text{m}$ for this non-optimal design.

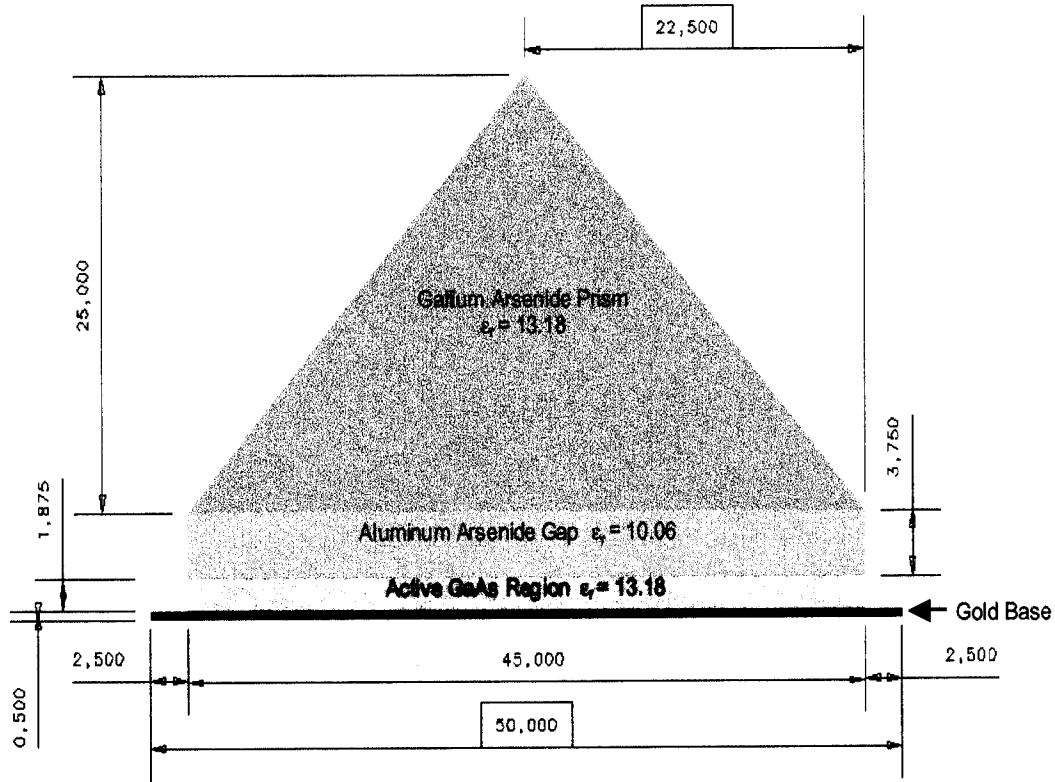


Figure 7. Geometry of prism coupler with aluminum arsenide gap layer. Relative permittivity values used in calculations are shown for the materials.

Shown in Figure 9 are electric field plots throughout the prism coupler for the two different aluminum arsenide-gap sizes. The wavelengths of operation for each simulation correspond to a peak energy level in Figure 8. In comparison to similar figures for the air-gap prism (Figures 4 and 6), electric fields in this aluminum arsenide-gap prism are not as well trapped in the active region. This is due to the lack of confinement in the gallium arsenide base region which acts as a waveguide structure when bounded by the air-gap above. As in the air-gap prism though, a discontinuity in the active region to the left and right of the base is considered essential to force trapping of the energy in the active region. This trapping of the energy is thought to form the resonant peaks in the energy coupling curves and when used in an active array also eliminates energy leaking from one pixel to the next as it propagates along the active region.

COMPARISON OF AIAs-GAP PRISM COUPLERS TO GRATING COUPLER

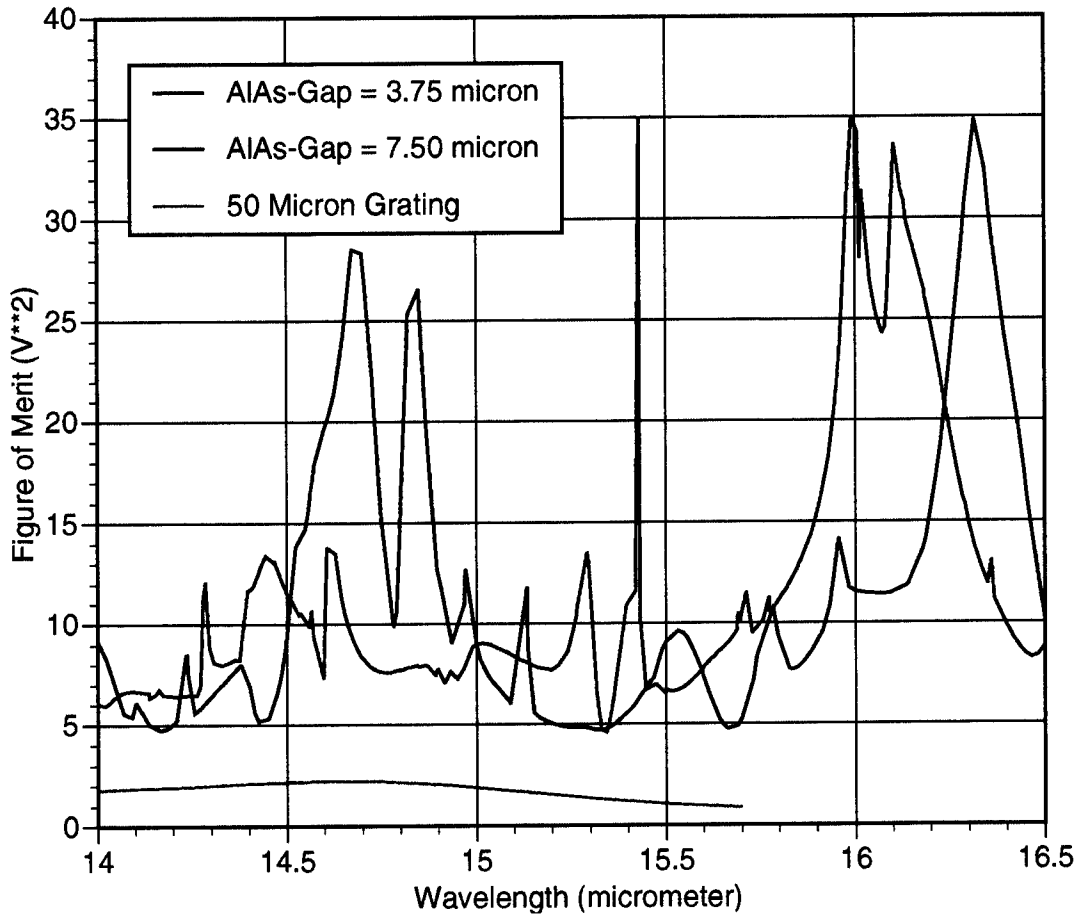


Figure 8. Comparison of figures of merit for aluminum arsenide-gap prism couplers shown in Figure 7 with optimized grating coupler. Two different gap thicknesses are shown.

VII. Conclusion

A new way to dramatically increase the sensitivity of quantum well infrared photodetectors has been found. It is based on the evanescent wave prism coupler originally developed for integrated optics applications. In this paper, it is used to change the polarization of an incident plane wave to a desired polarization that enhances absorption thereby improving greatly the sensitivity of this quantum well infrared photodetector. A specific design that allows monolithic fabrication has been proposed and its performance has been obtained by numerical simulation. A ten-fold increase in the sensitivity

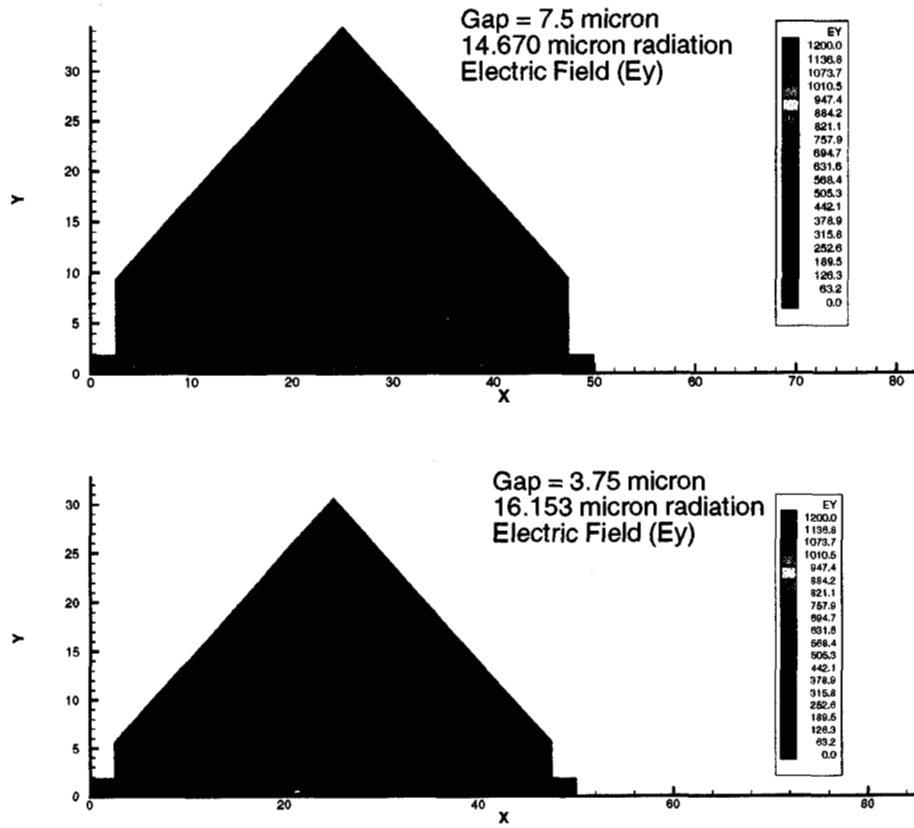


Figure 9. Electric field plots (E_y) for AlAs-gap prisms of different gap thicknesses. The wavelengths of operation correspond to peak figures of merit indicated in Figure 8.

over an optimized grating coupler at a given wavelength is demonstrated. By choosing the appropriate parameters such as the gap separation, the angle of the prism and the thickness of the quantum layer, it is possible to tune the maximum sensitivity of the detector to a given wavelength. Finally, it should be noted that the design given in this paper is aimed towards what can be implemented in practice.

VIII. Acknowledgments

The work described in this publication was carried out by the Jet Propulsion Laboratory, California Institute of Technology under a contract with the National Aeronautics and Space Administration. The supercomputer used in this investigation was provided by funding from the NASA Offices of Earth Science, Aeronautics, and Space Science.

IX. References

- [1] B. F. Levine, J. Appl. Phys. 74, R1 (1993)
- [2] S. D. Gunapala, J. S. Park, G. Sarusi, T. L. Lin, J. K. Liu, et al., IEEE-Device **44**, 45 (1997).
- [3] G. Sarusi, B. F. Levine, S. J. Pearton, K. M. S. Bandara, R. E. Leibenguth, Appl. Phys. **3L**, **64**, 960 (1994).
- [4] Y. C. Wang, S. S. Li, Journal Of Applied Physics, **74**, 2192 (1993).
- [5] J. Y. Andersson, L. Lundqvist, J-Appl-Phys, **71**, 3600 (1992).
- [6] T. R. Schimert, S. L. Barnes, A. J. Brouns, F. C. Case, P. Mitra, et al., Appl-Phys-L, **68**, 2846 (1996).
- [7] P. K. Tien, R. Ulrich and R. J. Martin, App Phys L, **14**, 291 (1969).
- [8] R. Shubert, and J Harris, IEEE Trans Antennas MTT, **16**, 1048 (1968).
- [9] T. Cwik, IEEE Trans Antennas Propag, **40**, 1496, (1992).
- [10] A. Poggio and E. Miller, Computer Techniques for Electromagetics., (Pergamon Press, London 1973) Chap. 4.
- [11] A. Glisson and D. Wilton, , IEEE Trans. Antennas Propagat., **28**, 593 (1980).
- [12] A. Borgioli, and T. Cwik, IEEE AP-S Intn Symp and URSI Radio Sci Mtg, Atlanta, GA (1998).
- [13] S. Adachi, Editor, "Properties of Aluminum Gallium Arsenide," (INSPEC, IEE, London 1993) Chap 5.